Aeroelastic behavior of a rotating semi-elastic double-swept rotor blade under climb conditions at the Rotor Test Facility Göttingen

Martin Müller
Research Scientist
Institute of Aeroelasticity
Göttingen, Germany

Armin Weiss
Research Scientist
Institute of Propulsion Technology
Cologne, Germany

Johannes N. Braukmann
Research Scientist
Institut of Aerodynamics and Flow Technology
Göttingen, Germany

C. Christian Wolf
Research Scientist
Institut of Aerodynamics and Flow Technology
Göttingen, Germany

ABSTRACT

The study presents the aeroelastic behavior of a double-swept rotor blade, that was investigated under climb conditions on a four-bladed rotor in the rotor test facility at the German Aerospace Center in Göttingen. The results of two measurement campaigns are combined to obtain a detailed insight in the coupling of blade deformation, integral loads, aerodynamic behavior and blade tip vortex. Especially the interaction between stall onset and blade tip vortex is in focus of the investigation. The first measurement campaign considered the underlying aerodynamics, integral blade loads and blade deformation by means of unsteady pressure-sensitive paint (iPSP), strain gauges at the blade root and blade tip marker. The blade tip vortex behavior was characterized in a second measurement campaign with particle image velocimetry (PIV). Different pitch settings were investigated at a rotation frequency of f_{rot} = 23.6 Hz, that corresponds to blade tip Mach and Reynolds numbers of M_{tip} = 0.282 - 0.285 and Re_{tip} = 5.84 - 5.95 x 10^5. The results reveal a detailed insight into a two-step stall behavior and its impact on blade flapping and torsion. The iPSP and PIV data indicates an interaction between stall onset at the blade tip and a simultaneous inward motion of the blade tip vortex caused by the backward-swept part of the blade.

NOTATION

a	Speed of sound (m/s)
b	Width of wind tunnel nozzle (m)
c	Blade chord length (c_{root} = 0.072 m)
C_pM^2	Radial pressure coefficient
C_T	Thrust coefficient
EI	Bending stiffness (Nmm^2)
f	Frequency (Hz)
GI	Torsional stiffness (Nmm^2)
h	Height of wind tunnel nozzle (m)
M	Mach number
p	Pressure (Pa)
R	Rotor blade radius (R= 0.65m)
Re	Reynolds number
r	Radial distance (m)
T	Thrust (N)
v	Flow velocity (m/s)
V	Blade velocity (m/s)
w	Velocity component in z-direction (m/s)
x	Chordwise distance form leading edge (m)
z	Rotor inflow direction (m)

Greek symbols

Θ	Blade pitch angle (deg)
ρ	Air density (kg/m^3)
σ	Rotor solidity (σ = 0.141)
Ψ_V	Tip vortex wake age (deg)
ω	Out-of-plane vorticity ($1/s$)

Subscripts

1,flap	First flap mode
2,flap	Second flap mode
i	Induced
tip	Blade tip
root	Root of the blade
rot	Related to rotor
∞	Axial inflow

Presented at the Vertical Flight Society's 79th Annual Forum & Technology Display, West Palm Beach, FL, USA, May 16–18, 2023.

INTRODUCTION

Vibration, noise, and performance characteristics of helicopter rotors can be optimized by innovative blade tip geometries. A well-known example is the BlueEdge rotor blade geometry that was developed in recent years. The tip shape has been derived from the ONERA-DLR “ERATO” design (Refs. 1,2). The forward-backward swept shape is mainly optimized to improve the rotor acoustics in forward flight. The backward sweep at the blade tip reduces the effective Mach number and also the drag on the advancing side. The parallel blade vortex interaction is also reduced and, thus, improves the rotor acoustics. Another example of an alternative blade tip geometry is the “paddle tip” from the British Experimental Rotor Programme (BERP). This blade tip was aerodynamically optimized for high-speed flight by using a larger blade tip area. Both tip designs have individual blade tip vortex, stall, and aeroelastic characteristics in comparison to common blade tip designs. The individual characteristics of each new design have to be investigated in detail.

The focus of most rotor blade studies in forward flight conditions is set on individual aspects only, such as aerodynamics (Ref. 3), noise, or blade deformation (Refs. 4, 5). The aeroelastic aspect mainly considers mode shape tracking, the monitoring of mode shape frequency increase, in the rotating system (Refs. 6–8). An additional, relevant aeroelastic topic is the interaction of blade loads, aerodynamic characteristics and blade deformation. Rather than highlighting a single aspect of innovative blade tip design, this paper focuses on the interaction between blade loads, aerodynamic characteristics and blade deformation. Recently published studies with two different double swept rotor blade models (Refs. 9,10) investigated the aeroelastic (Ref. 11) and aerodynamic (Refs. 12–15) characteristics during dynamic stall in a rotating system. The aeroelastic behavior in hover and slow climb conditions will be investigated in the current work.

The aeroelastic behavior impacts blade root forces and blade deformation, hence, also hover and forward flight performance. An aeroelastic study at the rotor test facility Göttingen (RTG) with a double swept subscaled model showed a nonlinear blade flap behavior mainly caused by the stall characteristics on the backward-swept part of the blade at investigated cyclic pitch cases. Also, the stall on the forward-swept part of the blade impacts the strength of the blade flap motion (Ref. 11). In addition a blade tip vortex study with the same blade tip model reveals a significant interaction between stall onset and the burst of the blade tip vortex at cyclic pitch test cases (Ref. 14). For slow climb condition the coupling effects and relation between stall, blade vortex burst and deformation are unknown. Therefore, in the current study a double swept rotor blade model was investigated regarding the aeroelastic behavior in slow climb condition at the RTG. For a detailed insight into the coupling effects, the results of two measurement campaigns were combined. The first campaign focused on the blade tip vortex characteristics, the second campaign investigated the surface pressure distribution in combination with integral blade loads and blade tip deformation. Both campaigns were conducted with equal test conditions. For the blade tip vortex study a high-speed particle image velocimetry (PIV) system was used. The surface pressure distribution was measured with unsteady pressure sensitive paint (iPSP) (Ref. 16). Here, the results of both studies are combined, with a particular view on aeroelastic topics. Focus of the aeroelastic analysis was the impact of stalled blade areas on the blade pitching moment, normal forces, and their position with respect to the elastic axis.

EXPERIMENTAL SETUP

Aeroelastic model properties

The blade planform, the radial distribution of the stiffness and the center of gravity can be seen in Fig.1 and Tab.1. The chordwise position of the elastic axis was identified by using strain gauges at the blade root. Two full bridge strain gauge configurations were used to measure the flap and torsion displacements, see Müller et al. (Ref. 11) for details.

Table 1: Sectionwise bending and torsional stiffness

Sections	EI, Nmm^2	GI, Nmm^2
S1	169.03	89.65
S2	84.61	37.77
S3	66.57	19.47

At three different radial positions calibration brackets were mounted at the rotor blade. For each mounting position the chordwise location of the elastic axis was identified, based on a decoupling between flap and torsion. Between the blade root

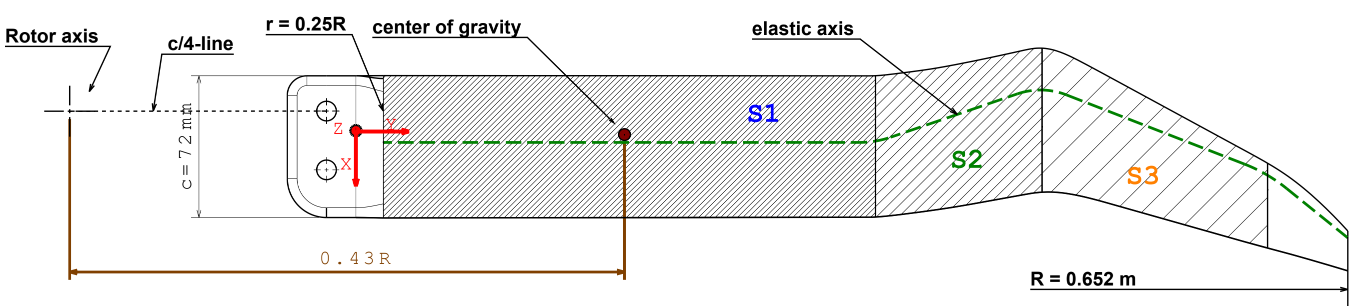

Figure 1: Elastic axis, center of gravity and stiffness distribution for three radial Sections (S1, S2, S3)

and the beginning of the forward-swept part, the elastic axis is at a constant chordwise location of $0.47c$. Further outboard, the elastic axis is shifted towards the leading edge, reaching $0.25c$ (local chord) at the end of the forward-sweep, and $0.11c$ (local chord) at the end of the backward-sweep. The shift towards the leading edge at the forward and backward-swept part are mainly caused by the structural design. The chord length tapers over the radius from c_{root} = 0.072 m at the root to c_{tip} = 0.020 m at the blade tip.
The double swept model has a weight of 236 g and the center of gravity was determined at $0.43R$ and $0.42c$. As can be seen in Tab.1, the model is stiff in comparison to its weight. This allows the assumption that inertial forces are negligible. Due to the high stiffness, the eigenmodes of the model are very high. The first flap was identified at $f_{1,\text{flap}}$ = 44.43 Hz in the non-rotating system. At a rotation frequency of f_{rot} = 25 Hz the first flap eigenmode increases to $f_{1,\text{flap}}$ = 53 Hz. Hence, at a rotation frequency of f_{rot} = 23.6 Hz there is no significant excitation of the first flap motion. The second eigenmode was identified at $f_{2,\text{flap}}$ = 177.14 Hz and also does not affect the blade motion.

Unsteady pressure sensitive paint

The experimental setup for the unsteady pressure sensitive paint measurement in the RTG can be seen in Fig.2. The nozzle of the Eiffel type wind tunnel has a cross section of 1.6 m $\times$ 3.4 m ($h \times b$) and an axial inflow of v_∞ = 2 m/s was used to prevent recirculation of the rotor flow in the test chamber. The rotor axis is oriented horizontally, and the rotor plane is located 2.3 m downstream of the wind tunnel nozzle. The RTG was mainly developed for dynamic stall (Refs. 17–19) and slow climb (Ref. 20) investigations. A fully functional swashplate allows collective and cyclic pitch cases. The integrated measurement system of the RTG is a telemetry system for sensors built into the rotating system (pitch sensors, strain gauges, etc.). For the measurements a double-swept rotor blade tip model on a four-bladed rotor with a radius of R = 0.652 m was used. More information about twist, chord length distribution, instrumentation and sweep are presented in (Refs. 10, 11). All presented test cases were measured under the following conditions: f_{rot} = 23.6 Hz, M_{tip} = 0.282 - 0.285 and Re_{tip} = 5.84 - 5.95 $\cdot$ 10^5. The collective pitch angles were varied from Θ_{root} = 6° - 38°, with an increment of 1°. Surface pressure results were obtained by averaging 128 individual results acquired during 256 blade revolutions for collective test cases. The unsteadiness of the paint was exploited for the cyclic pitch cases which are discussed elsewhere, see (Refs. 11, 16). For the iPSP measurements the aerodynamic airfoil of one of the rotor blades was coated with unsteady pressure sensitive paint from $0.35 \leq r/R \leq 1$. The iPSP sensor provides unsteady surface pressures with a -3dB cutoff frequency of 6 kHz (Refs. 21,22). For the iPSP illumination a laser with corresponding optics was placed under the wind tunnel nozzle, Fig.2. The image acquisition was done with a camera (FoxCam4M) (Refs. 23,24), placed almost centrally under the wind tunnel nozzle. For more details about the iPSP measurement technique and experimental setup, see Ref.15. The inflow velocity was measured by using a Prandtl-probe in the nozzle. A six-component piezoelectric balance measured the rotor thrust. The blade flap displacement was measured with a blade tip camera, flash LED and retroreflective blade tip markers. For each collective test case 50 blade tip images were acquired and averaged. The integral blade

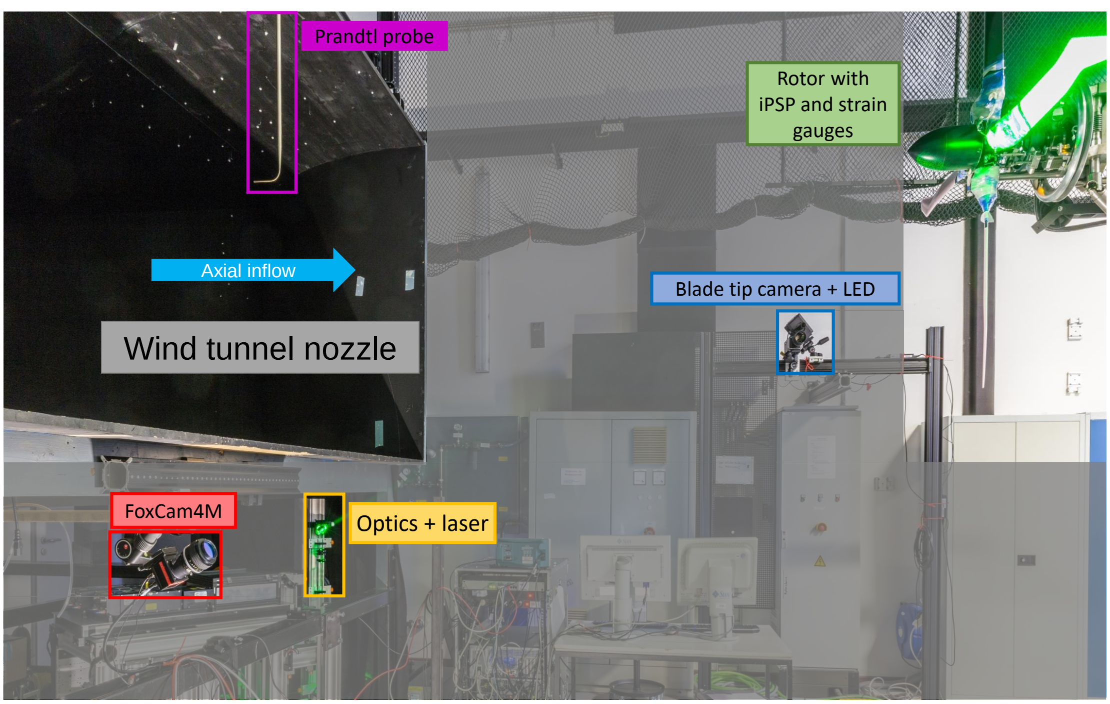

Figure 2: Image of the experimental iPSP setup at the Rotor Test Facility Göttingen (Ref. 11)

root forces and moments were measured with strain gauges in two full bridge configurations. More information about measurement technique synchronization, sample rate, image analysis is presented in Ref.11, 16.

Particle image velocimetry

Figure 3 displays the experimental setup for the particle image velocimetry (PIV) measurement. A detailed description of the experimental setup and analysis approach is presented in (Ref. 14). In the following a short summary is given. The experiment was conducted in the RTG under nearly the same conditions as mentioned in the section Unsteady pressure sensitive paint. For the PIV measurement, the rotor frequency was slightly increased to $f_{\text{rot}} = 24$ Hz due to frequency limitations of the phase-locked PIV laser. However, the results discussed in this paper are normalized to the blade tip velocity, and the small difference in the Reynolds/Mach numbers are negligible. The non-dimensional rate of V_∞/V_{tip} is 0.022. Due to the role of the blade tip vortex at stall onset, the results of two collective pitch cases ($\Theta_{\text{root}} = 24°$ and $26°$) were selected to illustrate the structure of the corresponding blade tip flow.

A PIV system was used to provide the velocity distribution in an axial-radial slice plane just downstream of the rotor plane to visualize the rotor wake flow, see Fig.3. For the experiment a double-pulse laser was used to illuminate the aerosolized oil droplets. The light sheet was generated with the corresponding optics. Due to non-recirculation inflow and low pulse energy of the lasers, a large rate of tracer particle generation is needed to generate a sufficient seeding quality. Therefore, four seeding devices were placed upstream of the wind tunnel fan. The seeding devices produce droplets with a diameter between approx. 1 μm and 2 μm. For a reduced size of particle voids in the tip vortex center due to centrifugal forces, small droplets are important. The stereoscopic layout was set up with two double-frame cameras, mounted left and right below the test stand. For the raw image analysis an iterative PIV cross-correlation algorithm was used. The high-speed laser and cameras were phase-locked to the rotor and acquire double-images for a wake age of $\Psi = 10°$ after the passage of the blade's trailing edge. For each test condition, 450 flow samples were recorded.

RESULTS

Figure 4 displays a collective pitch thrust polar of the double-swept rotor blade (DST) for a rotational frequency of $f_{\text{rot}} = 23.6$ Hz (red). In addition, the depicted blue dots represent the data for the increased rotor frequency of $f_{\text{rot}} = 24$ Hz. The collective thrust polar shows the specific blade loading C_T/σ against the blade root pitch angle Θ_{root}. The specific blade loading is defined as

$$C_T/\sigma = \left(\frac{T}{\rho \pi R^2 V_{tip}^2}\right)/\sigma \qquad (1)$$

The thrust increases linearly up to $\Theta_{\text{root}} = 24°$. This indicates continuously increasing lift over the blade and no evidence for stall or other non-linear aerodynamic effects in the first section of the thrust polar, see Fig.4. From label a) to label b) in Fig.4 a reduced gradient of C_T/σ is noted in comparison to the first section. The maximum thrust is reached at label b). The two kinks in the thrust slope at labels a) and b) indicate a two-step stall behavior, with a still increasing thrust between a) and b), but a decreasing thrust beyond b). The first part of the stall is caused by tip separation involving the tip vortex, more details are given in (Refs. 14, 16). This

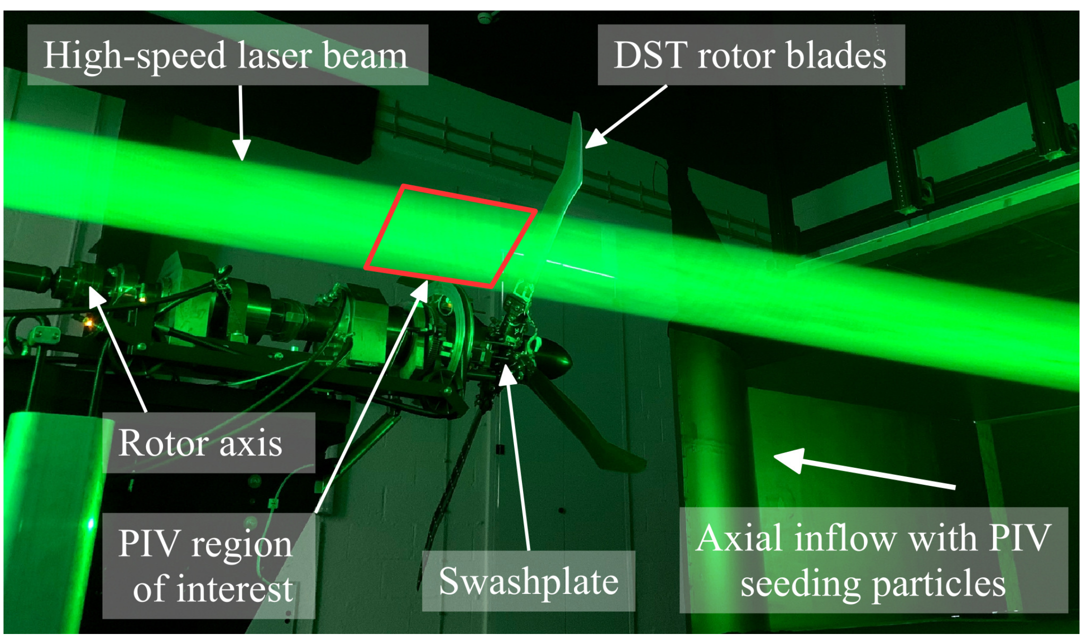

Figure 3: Image of experimental PIV setup at the RTG in Göttingen, modified from Wolf et al. (Ref. 14)

specific stall behavior also impacts the aeroelastic behavior regarding pitching moment, blade normal force and deformation. Especially the stall evolution over the suction side in the backward-swept part is relevant for the blade pitching moment, due to the distance between low-pressure regions and the elastic axis.

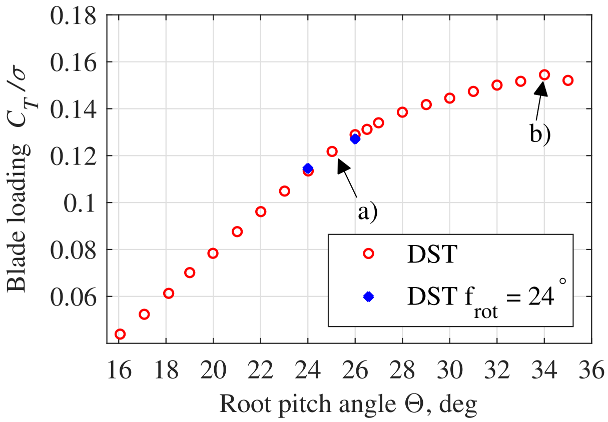

Figure 4: Specific blade loading against pitch angle, modified from Wolf et al. (Ref. 14)

The measured thrust coefficients for the f_{rot} = 24 Hz PIV test cases are $C_{T_{24^\circ}}$ = 0.01615 and $C_{T_{26^\circ}}$ = 0.01792. The resulting specific blade loading are $C_{T_{24^\circ}}/\sigma$ = 0.11454 and $C_{T_{26^\circ}}/\sigma$ = 0.12710, see Fig.4 (blue). The relative thrust deviations between 23.6 Hz and 24 Hz rotor frequencies are 1% at 24° and 1.5% at 26° root pitch angles. This is within the error margin of the force balance system, and the comparability of the iPSP and PIV results is given.

Blade deformation and integral loads

In Fig.5 the elastic blade tip deformation (plot a) and the integral blade root loads (plot b) are shown. The elastic deformation (plot a) is shown by means of the flap displacement (blue line) and the elastic torsion angle (green line) against the blade root pitch angle Θ_{root}. Both quantities were measured with the blade tip camera. The right plot (b) in Fig.5 shows the integral blade loads by means of the root normal force (blue line) and the pitching moment (green line) against blade root pitch angle Θ_{root}. The blade root normal force is defined as the acting force normal to the chord at $0.3R$ and $0.35c$ due to the strain gauges position. For a better visualization of the gradient trend, the linear section (Θ_{root} = 14° - 24° in Fig.5) of the normal force and flap displacements were extrapolated, depicted as red dashed lines in Fig.5. The values for each test case were averaged over 450 revolutions. The trend of the blade pitching moment shows three interesting features: 1. slight dip at small pitch angles, 2. strong dip coincidental with stall onset around Θ_{root} = 24°, 3. sharp increase shortly before the second stall at Θ_{root} = 34°.

At Θ_{root} = 8° - 12° a slight dip in the blade root pitching moment can be seen (Fig.5b). However, the trend of the elastic torsion (Fig.5a) does not reflect this dip. Due to the high torsional stiffness the acting pitching moment is not sufficient to generate an elastic torsion. The dip is probably connected to the change from negative to positive thrust, which depends on the radial position along the blade and the corresponding local pitch angle. Also, the trend of the normal force (Fig.5b) and flap displacement (Fig.5a) indicate a transition process from negative to positive blade flap and normal force values with a reduced gradient.

Around stall onset at Θ_{root} = 24° - 25° a reduced gradient in the trend of blade normal force and blade flap can be observed, see Fig.5. This also correlates well with results of Wolf et al. (Ref. 14) and Weiss et al. (Ref. 16) for stall onset. Thus, the reduced aerodynamic lift force results in a reduced flap displacement. The rotor blade reacts instantly to changing acting forces. These are the properties of an ideal stiff blade (Refs. 25, 26). This means the displacement follows the acting force instantaneously. Another indicator for the stall onset is the increasing standard deviation of the normal force due to increasing aerodynamic unsteadiness at Θ_{root} = 25°. A further increase of the root pitch angle up to Θ_{root} = 34° continuously increases the normal force's standard deviation, shown as vertical error bars, underlining an increasing influence or strength of the developing flow separation, see Fig.5b. It is noted that the stall behavior in Fig.5 mirrors the behavior of the specific blade loading discussed in Fig.4. The blade

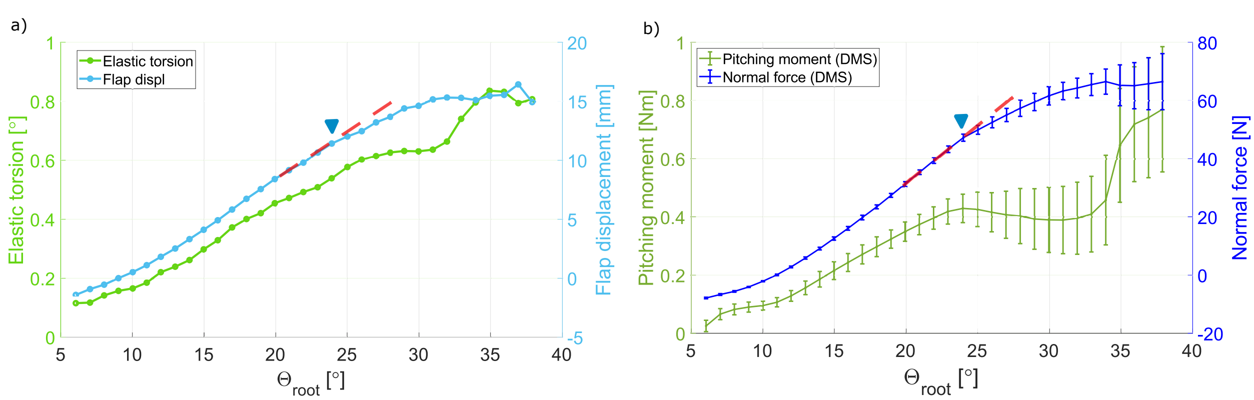

Figure 5: Elastic flap and torsion (a) and pitching moment and normal force (b) for Θ_{root} = 6° - 38° with extrapolation of the gradient trend as red dashed line for the normal section force and flap displacement and visualization of stall onset as blue triangle

pitching moment reveals a strong dip around Θ_{root} = 23° - 27°. The drop of the blade pitching moment also impacts the elastic blade torsion. From Θ_{root} = 24° up to Θ_{root} = 31° a slight decrease of the pitching moment can be seen, Fig.5b. The elastic torsion slightly follows the trend of the pitching moment. The gradient of the elastic torsion almost drops to zero at Θ_{root} = 26° and increases again at Θ_{root} = 32°, see Fig.5a. The strong changes in the pitching moment only result in small changes of the elastic torsion, which can be attributed to the high stiffness of the blade. The increasing standard deviation of the pitching moment between Θ_{root} = 24° - 34° is again connected to an increasing aerodynamic unsteadiness due to the stall build-up. The comparably high standard deviation of the pitching moment even under attached-flow conditions is caused by the higher fluctuation in the pitching moment.
At high pitch angles around Θ_{root} = 34° - 35° a second drop of the blade normal force can be seen, Fig.5b. The second drop can also be observed in the specific blade loading, see label b) in Fig.4. Thus, the two-step stall also affects the normal force. The maximum blade flap displacement is reached slightly earlier at Θ_{root} = 32°, see Fig.5a. This is caused by the high stiffness of the first and second blade section in relation to the third blade section, see Fig.1. A more detailed explanation is provided in the section on High pitch angles. A sharp increase can be observed in the pitching moment and the elastic torsion between Θ_{root} = 33° - 36°. This increase is mainly caused by aerodynamics and will be explained in the section on High pitch angles.

Small pitch angles

In the following section the aerodynamic results and their impact on the blade behavior are presented. In Figs.6, 8, 9 the radial surface pressure distributions are depicted as C_pM^2. In

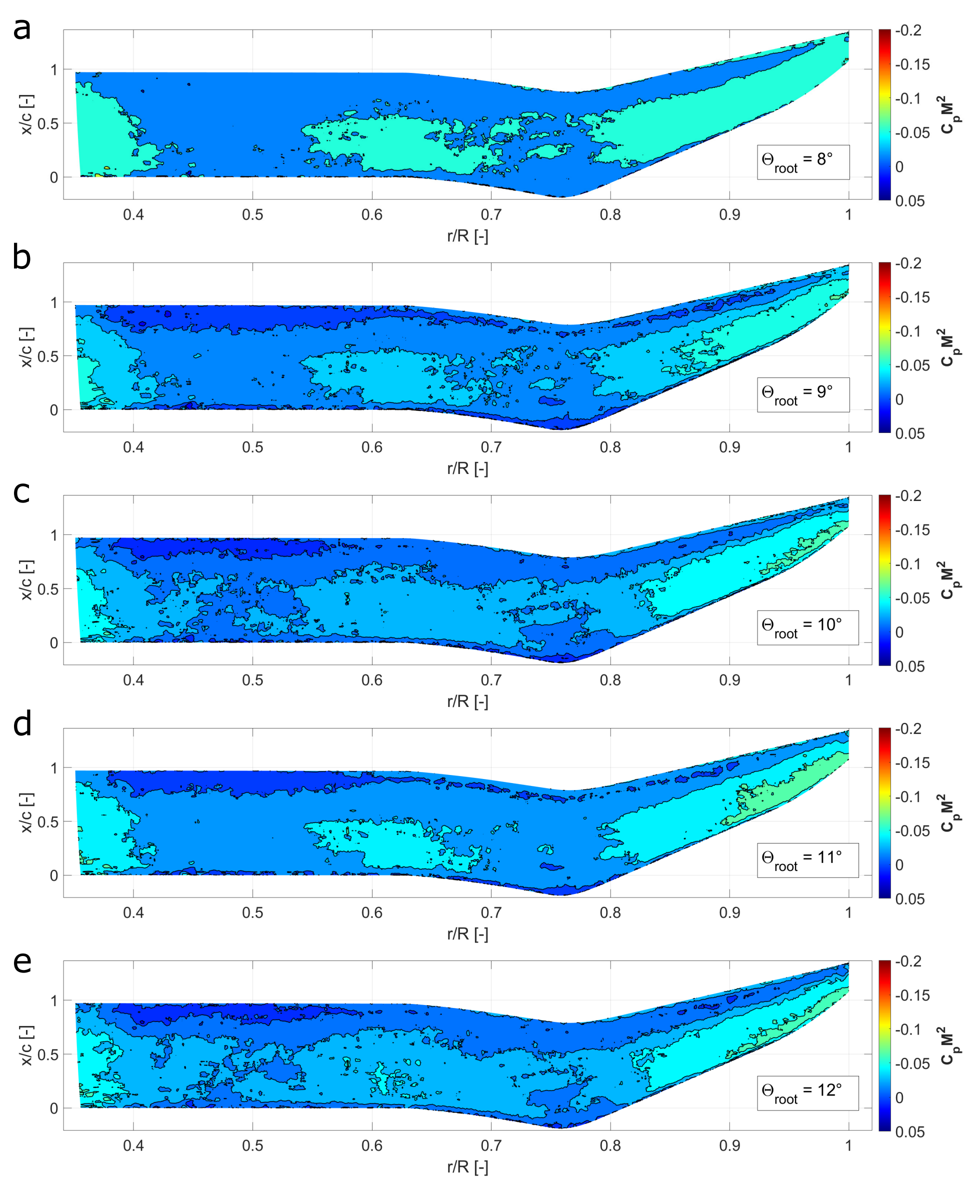

Figure 6: Surface pressure maps as C_pM_2 for Θ_{root} = 8° - 12°.

each figure, five different collective pitch test cases are shown. In addition, the pressure distributions are compared to the integral blade loads and deformations in Fig.5. The surface pressure coefficient is defined as

$$C_p M^2 = \frac{p - p_\infty}{\rho_\infty/2 \cdot {a_\infty}^2}, \tag{2}$$

For small pitch angles, at Θ_{root} = 8° (Fig.6a) large areas of the blade show pressure coefficients $C_p M^2$ slightly above zero (blue). Especially the area around the kink ($0.7 \leq r/R \leq 0.8$) as well as a part of the straight section $0.43 \leq r/R \leq 0.56$ (Fig.6a) indicate downforce. In contrast the backward-swept part ($0.8 \leq r/R \leq 1.0$) and parts of the forward-sweep ($0.6 \leq r/R \leq 0.7$) feature slightly negative $C_p M^2$ values. This results in lift-generating sections, where nose up (positive) pitching moments are induced and downforce-generating sections, where nose down (negative) pitching moments are induced. In addition the elastic axis shifts towards the leading edge in the outer forward-backward swept parts, see Fig.1. This leads to a decreasing lever arm with respect to the leading edge with increasing radius. Finally, the nose up and nose down pitching moments compensate each other, leading to a near-zero but slightly positive integral blade root pitching moment, see Fig.5. At Θ_{root} = 9° (Fig.6b) a decrease of $C_p M^2$ in the backward-swept part can be observed ($0.88 \leq r/R \leq 1.0$), which generates a slightly higher nose up pitching moment due to the short lever arm with respect to the elastic axis. Additionally, $C_p M^2$ increases at the leading edge around the kink ($0.76 \leq r/R \leq 0.77$). That generates a weak downforce in combination with a large lever arm. At Θ_{root} = 10° (Fig.6c) a further decrease of $C_p M^2$ can be seen, near to the leading edge at the tip ($0.93 \leq r/R \leq 1.0$). In combination with the generated downforce around the kink ($0.76 \leq r/R \leq 0.77$), this leads to a plateau of the pitching moment and a reduced gradient of the normal force, see Fig.5b. Furthermore, the acting normal force affects the flap displacement, which also leads to a reduced gradient. The acting normal force transmits on the flap displacement, which leads also to a reduced gradient. The elastic torsion reveals no effect on the pitching moment due to the high torsional stiffness in sections S1 and S2, see Fig1. The largest share of the pitching moment is generated at blade parts with high torsional stiffness. Hence, no significant torsion can be observed. When further increasing the blade pitch angle to Θ_{root} = 11° (Fig.6d), the lift generating areas continue to grow, especially at the leading edge on the backward-swept part ($0.9 \leq r/R \leq 1.0$) and on the forward-swept part ($0.6 \leq r/R \leq 0.7$). This results in an increase of pitching moment, normal force and flap displacement, see Fig.5. The pitch angle of Θ_{root} = 12° is mostly dominated by a nose-up pitching moment over the entire radius.

Stall onset

As already discussed in Fig.5, the stall onset is characterized by a drop in the normal force, and discontinuities in the pitching moment and blade deformation. The difference in contrast to small pitch angles is that the blade deformations are affected by the normal force and the pitching moment. In addition, for two test cases (Θ_{root} = 24° and for Θ_{root} = 26°) the instantaneous streamwise velocity and the phase-averaged vorticity of the rotor wake including four blade tip vortices are depicted in Fig.7. The results were acquired 10° after a blade has passed the PIV measurement plane, hence, the vortex ages are Ψ_v = 10°, 100°, 190°, and 280° (left to right), since they were produced by a four-bladed rotor. The rotor plane is located at x/R=0.

At Θ_{root} = 23° (Fig.8a) a pronounced low-pressure region can be seen on the backward-swept part at the leading edge ($0.83 \leq r/R \leq 1.0$). The $C_p M^2$ value of the low-pressure region decreases with increasing radius. The footprint of the blade tip vortex is a thin, streamwise low-pressure line at the tip. For this pitch angle there are no indications for stall onset. This is also reflected in the normal force, pitching moment and blade deformation, see Fig.5.

When increasing the pitch angle to Θ_{root} = 24° (Fig.8b), no significant changes can be observed in the $C_p M^2$ distribution. The only change is a slightly more pronounced low-pressure region at the leading edge between $0.8 \leq r/R \leq 1.0$. The normal force and blade deformation reveal no significant changes in their trend, see Fig.5. The trend of the pitching moment shows a slightly decreasing gradient between Θ_{root} = 23° to Θ_{root} = 24°, suggesting a change in the flowfield around the blades. Figure 7a shows the phase-averaged flowfield of the wake at Θ_{root} = 24°. The inflow of the blades is steady and the flow direction is left to right. The coloring represents the out of plane velocity component w, for detailed information see Wolf et. al (Ref. 14). The slipstream boundary divides the flowfield into the external flow (upper part) and the rotor wake (lower part). The boundary is curved due to the wake contraction. In the slipstream boundary, four clear spatially concentrated tip vortices can be seen Fig.7a. In addition, Fig.7c shows the instantaneous and normalized out-of-plane vorticity ω for Θ_{root} = 24°. Four tip vortices can be identified as circular dots with positive rotation (Ref. 14). As mentioned in Wolf et. al (Ref. 14), "The youngest (leftmost) tip vortex blends into the corresponding blade shear layer, which at this age appears as a straight and vertical structure. The shear layer gradually transitions from counterclockwise rotation (yellow, upper part) to clockwise rotation (blue, lower part) in the radial region of the blade's thrust maximum, r/R = 0.75 - 0.90". These findings correlate very well with the iPSP result in figure 8b, that also indicates a radial region of the blade's maximum thrust at r/R = 0.75 - 0.90 (backward-swept part). Additionally, there is a good correlation with the normal force and flap displacement. In conclusion all measurement techniques verify the assumption of fully attached flow for this pitch angle.

If the pitch angle increases to Θ_{root} = 25° (Fig.8c) first indications of stall onset can be seen near the blade tip. The footprint of the blade tip vortex has moved further inboard when compared to Θ_{root} = 24° and is now represented as a broader, slanted low-pressure area initiated at the leading edge around r/R = 0.98 (Ref. 14). This stall onset also affects the normal force, pitching moment and flap displacement, see Fig.5. The

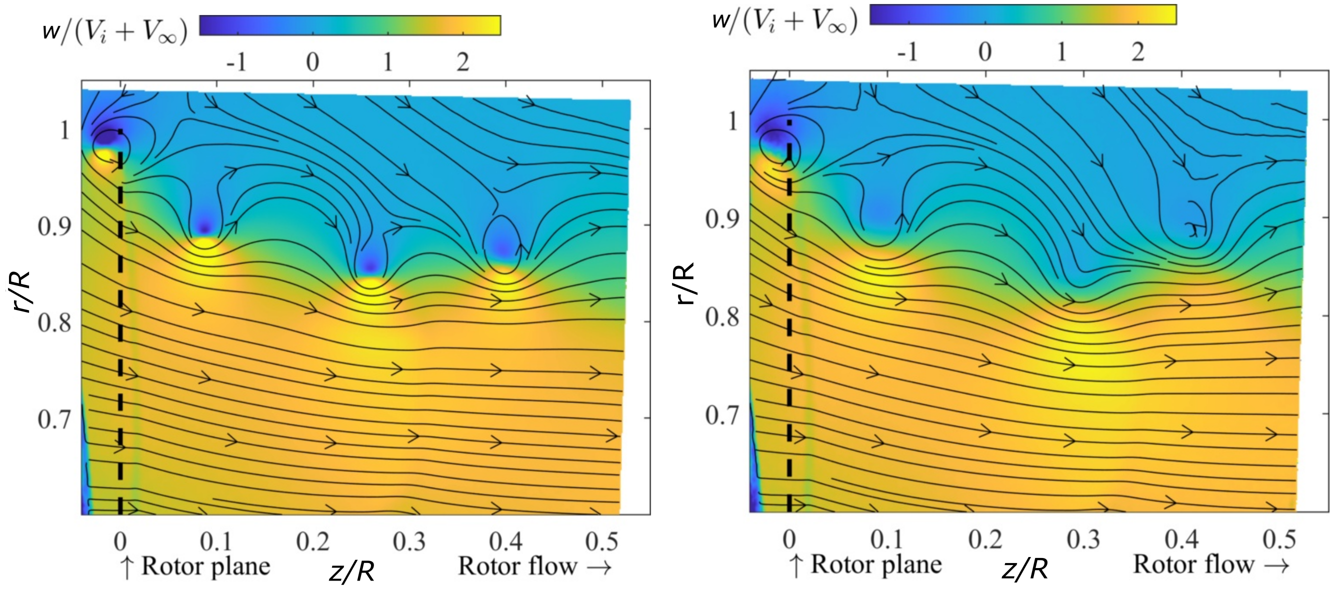

(a) DST rotor, phase-averaged streamwise velocity w for $\Theta_{root} = 24^\circ$, age of the leftmost vortex $\Psi_v = 10^\circ$

(b) DST rotor, phase-averaged streamwise velocity w for $\Theta_{root} = 26^\circ$, age of the leftmost vortex $\Psi_v = 10^\circ$

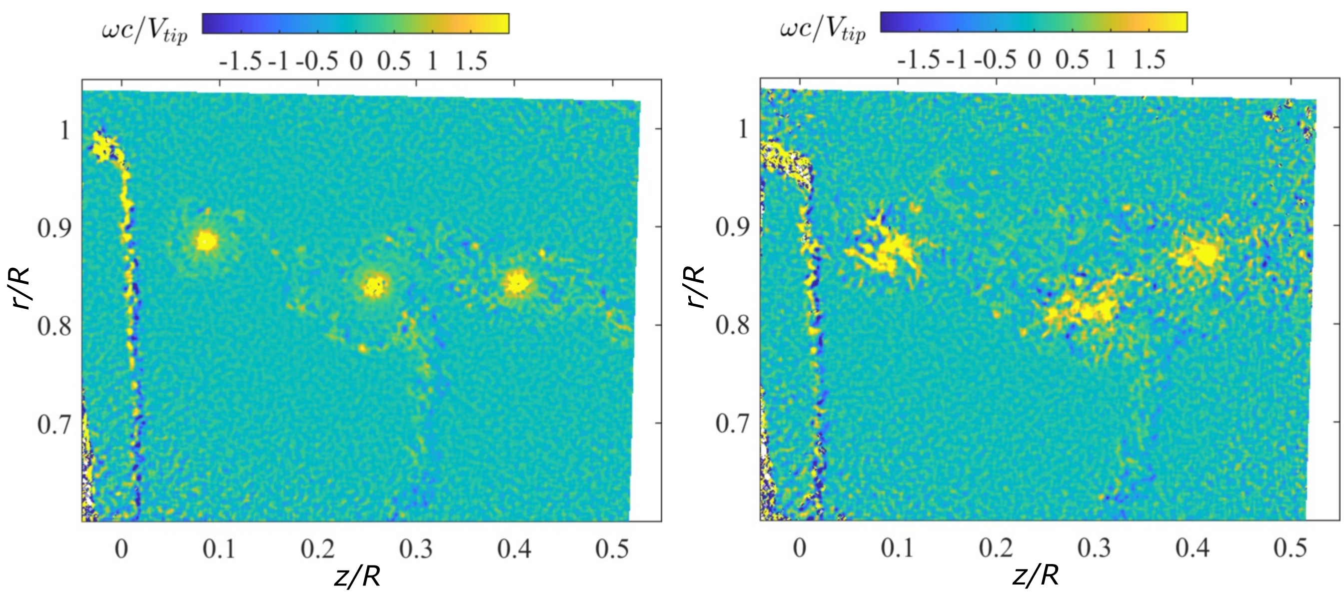

(c) DST rotor, instantaneous vorticity ω for $\Theta_{root} = 24^\circ$, age of the leftmost vortex$\Psi_v = 10^\circ$

(d) DST rotor, instantaneous vorticity ω for $\Theta_{root} = 26^\circ$, age of the leftmost vortex$\Psi_v = 10^\circ$

Figure 7: PIV results of the rotor wake for $\Theta_{root} = 24^\circ$ and $\Theta_{root} = 26^\circ$.

gradient of the normal force and flap displacement decreases from $\Theta_{root} = 24^\circ$ to $\Theta_{root} = 25^\circ$ caused by the loss of lift at the blade tip due to stall onset. In addition, the backward-swept part of the rotor blade reacts instantly to the loss of lift due to low bending stiffness in this area, see Fig.1 and Tab.1. The situation is different for the pitching moment and elastic torsion. The pitching moment decreases from $\Theta_{root} = 24^\circ$ to $\Theta_{root} = 25^\circ$, in contrast to the elastic torsion. The reason for this is the position of the elastic axis in this blade part. Due to the short lever arm from the elastic axis to the leading edge at the parabolic arc, the pitching moment is small and not sufficient to affect the elastic torsion. A further increase of the blade pitch angle up to $\Theta_{root} = 26^\circ$ (Fig.8d) shows a continuous motion of the vortex footprint inboard towards r/R=0.95, also connected to a further development of the stall in the backward-swept part of the blade tip. This is also reflected in the PIV results for $\Theta_{root} = 26^\circ$, see Fig.7b and Fig.7d. The comparison of the phase-averaged stream-

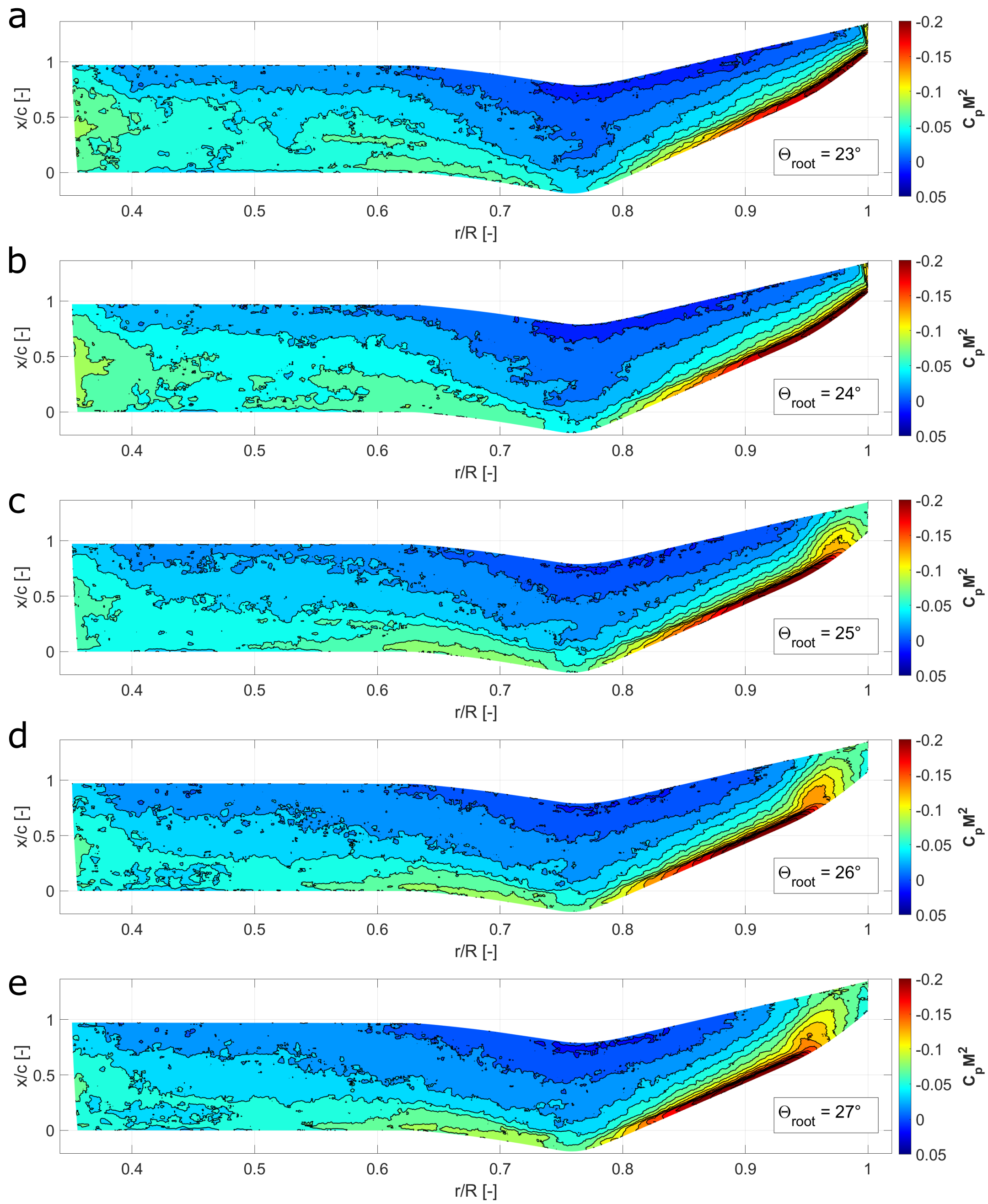

Figure 8: Surface pressure maps as C_pM_2 for Θ_{root} = 23° - 27° (Ref. 15).

wise velocity w between Θ_{root} = 24° and Θ_{root} = 26° reveals a significant wash-out of the flow structures, see Fig.7a and Fig.7b. Larger, and spatially less concentrated vortices show up as well as a higher aperiodicity. Additionally, the instantaneous vorticity ω reveals less concentrated tip vortices, with a beginning vortex bursting at the blade tip for (Θ_{root} = 26°), see Fig.7d. Nevertheless, thrust is still generated at 26° (even greater thrust than at 24°), so positive vorticity (counterclockwise in this figure) is still shed into the wake. The "wash-out" blade tip vortex structure at $\Psi = 10°$ and the blade shear layer indicate a slightly shifted blade's maximum thrust at r/R = 0.75 - 0.95. These findings in the PIV result correlate well with the iPSP data and indicate stall at the backward-swept part. The normal force and flap displacement are affected in the same way like at Θ_{root} = 25°. Due to a loss of lift, the gradients of the normal force and flap displacement decrease, see Fig.5. A slight change can be observed in the coupling between pitching moment and elastic torsion. The pitching moment decreases between Θ_{root} = 25° and Θ_{root} = 26°. In parallel, the gradient of the elastic torsion is decreasing due to the inward motion of the vortex footprint. Both the pitching moment and the gradient of the elastic torsion decrease between Θ_{root} = 25° and Θ_{root} = 26°, due to the tip vortex movement in inboard direction. In addition to the effect of the larger area of separated flow, the distance between the leading edge and the elastic axis increases towards the blade root, which further intensifies the effect on the pitching moment loss.

At $\Theta_{\text{root}} = 27°$ (Fig.8e) a further inboard motion of the vortex footprint can be seen. This behavior reinforces the coupling of the normal force to flap displacement and pitching moment to elastic torsion. The gradient of normal force and flap displacement decreases and the elastic torsion increasingly follows the pitching moment, see Fig.5.

High pitch angles

At high pitch angles, further coupling effects become apparent. As can be seen at $\Theta_{\text{root}} = 33°$ (Fig.9a) the vortex footprint extends over a large area of the backward-swept part. The footprint starts at the leading edge at $r/R = 0.86$. The inward motion of the vortex footprint leads to detached flow in the area of the tip ($0.92 \leq r/R \leq 1.0$). This leads to a loss of lift in the softest part of the blade with respect in terms of bending stiffness. The maximum flap displacement is reached around $\Theta_{\text{root}} = 32°$, see Fig.5a. Furthermore, the gradient of the normal force decreases in comparison to $\Theta_{\text{root}} = 32°$. A second, weaker low-pressure region has developed at the leading edge of the forward-swept part ($0.66 \leq r/R \leq 0.74$). Due to the longer lever arm from the elastic axis to the low-pressure region in the kink region the pitching moment starts to increase again.

This behavior continues when the pitch angle increases up to $\Theta_{\text{root}} = 34°$ (Fig.9b). The vortex footprint continues to move inward and the low-pressure regions at the forward-swept part increase. This leads to an increase of the normal force but not

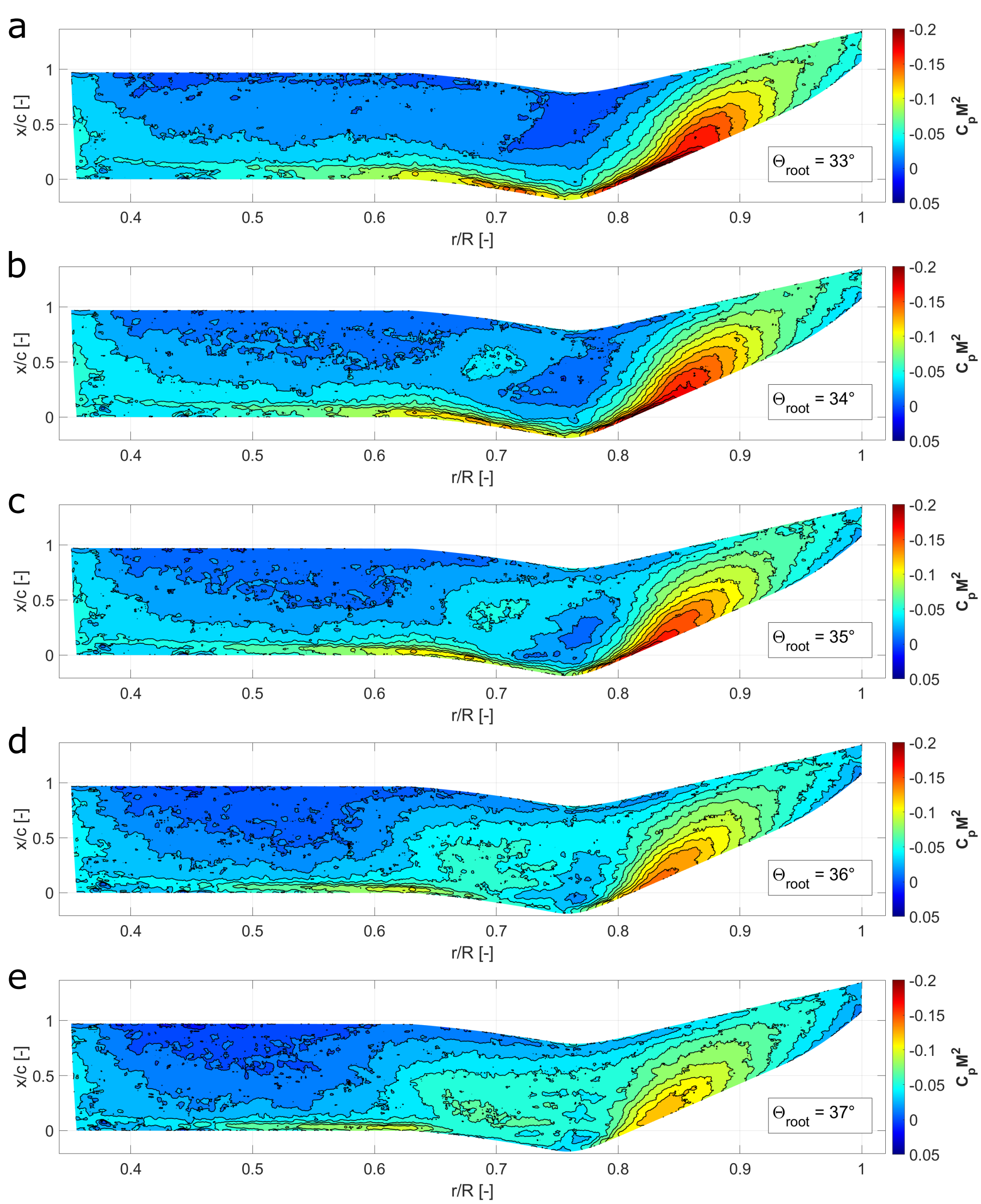

Figure 9: Surface pressure maps as C_pM_2 for $\Theta_{\text{root}} = 33°$ - $37°$.

to an increase flap displacement, see Fig.5. The pitching moment and elastic torsion also increase due to the high discrete pitching moment generated from the low-pressure regions at the leading edge in and outboard of the kink.
If the pitch angle increases to $\Theta_{\mathrm{root}} = 35°$ (Fig.9c) the vortex footprint weakens slightly in the backward-swept part. The low-pressure regions at the leading edge inboard of the kink and between $0.58 \leq r/R \leq 0.7$ generate an increase of the pitching moment and elastic torsion, due to the increased lever arm, see Fig.1. The integral normal force decreases simultaneously, see Fig.5b.
At $\Theta_{\mathrm{root}} = 36°$ (Fig.9d) a further weakening of the vortex footprint in the backward-swept part can be observed. Additionally, the suction peak at the leading edge of the kink decreases. This leads to a further decrease of the normal force and a constant flap displacement. Also, the gradient of the pitching moment decreases with a parallel drop of the elastic torsion.
The pressure distribution at $\Theta_{\mathrm{root}} = 37°$ (Fig.9e) reveals an even weaker vortex footprint (with larger pressures) across the backward-swept part of the blade. Moreover, large areas of the forward and backward-swept parts show detached flow.

CONCLUSIONS

The aeroelastic behavior of a four-bladed rotor with an innovative double-swept rotor blade model was investigated under slow climb conditions, close to hover conditions, in the rotor test facility Göttingen. The results of two measurement campaigns were combined for a detailed insight in the areoelastic behavior. For this purpose, the blade deformation, integral blade loads, surface pressure distribution and velocity fields of the blade tip vortices were investigated. Especially the interaction between stall onset and inward motion of the blade tip vortex were in focus. The main result of the study can be summarized as follows:

1. The double-swept planform shows a two-step stall behavior which is reflected in the polars of the integral blade normal force, flap displacement, pitching moment and elastic torsion. The rotor blade can be assumed as ideally stiff.
2. In the trends of the pitching moment and the normal force, three different pitch-dependent intervals with different phenomena can be identified: 1. at small pitch angles, 2. at stall onset, 3. at high pitch angles:
    3. At small pitch angles a slight dip in the pitching moment and a reduced slope of the normal force and flap displacement can be observed. Due to the location of the elastic axis close to the blade tip, the change in pitching moment does not affects the elastic torsion.
    4. During the stall onset a strong dip in the pitching moment and the elastic torsion can be identified. The resulting integral pitching moment depends on the location of the elastic axis to corresponding low pressure areas. Additionally, the normal force and flap displacement show a continuously decreasing slope which goes along with an inboard motion of the detached blade tip vortex footprint.
5. The section at high pitch angles reveals that the maximum flap displacement is reached prior to the maximum normal force. This is due to the flexible backward-swept part of the blade in combination with flow separation in the same region. The pitching moment as well as elastic torsion increases shortly before complete stall at the forward and backward-swept part.

ACKNOWLEDGMENTS

Funding of the DLR project URBAN Rescue is gratefully acknowledged. The authors would like to thank T. Büte and M. Krebs (DLR Göttingen) for all the support in the measurement campaigns and C. Stieg (DLR Göttingen) for his support during model preparation.

REFERENCES

1. Splettstroesser, W.R., Prieur, J., Pahlke, K., Schultz, K.-J., van der Wall, B.G., Delrieux, Y., Gardarein, P., Geoffroy, P., and Leconte, P., "Investigation of young blade-tip vortices at a rotor test facility using stereoscopic PIV," *DLR Internal Report, DLR-IB 129-97/10*, Braunschweig, 1997.

2. Delrieux, Y., Prieur, J., Costes, M., Gardarein, P., Beaumier, H., des Rochettes, H.M., Leconte, P., Crozier, P., Splettstroesser, W.R., van der Wall, B.G., Junker, B., Schultz, K.-J., Mercker, E., Pengel, K., Philippe, J.J., and Gmelin, B., "The ONERA-DLR Aeroacoustic Rotor Optimisation Programme ERATO: Methodology and Achievements," *American Helicopter Society Aerodynamics, Acoustics and Test and Evaluation Technical Specialists Meeting*, San Francisco, 2002.

3. Bauknecht, A., Wang, X., Faust, J-A. and Chopra, I., "Wind Tunnel Test of a Rotorcraft with Lift Compounding," *Journal of the American Helicopter Society*, Vol. 66, 2021 , doi: 10.4050/JAHS.66.012002.

4. Abrego, A. I., Meyn, L., Burner, A. W., and Barrows, D. A., "Summary of Full-Scale Blade Displacement Measurements of the UH-60A Airloads Rotor," *AHS Technical Meeting on Aeromechanics Desgin for Vertical Lift*, 20-22 January, San Francisco, California, 2016.

5. Schairer, E. T., Heineck, J. T., and Spooner, H., "Blade Displacement Measurements of a Rotor in Forward Flight in the Langley 14- by 22-Foot Wind Tunnel," *AIAA SciTech Forum*, 19-21 January, Virtual Event, 2021.

6. Rizo-Patron and Sirohi, J., "Operational Modal Analysis of a Helicopter Rotor BladeUsing Digital Image Correlation," *Experimental Mechanics*, Vol. 57, 2017, DOI 10.1007/s11340-016-0230-6.

7. Rohin Kumar, M. and Lokeswara Rao, V., "Aeroelastic analysis of double-swept rotor blade in hovering conditions," *International Forum on Aeroelasticity and Structural Dynamics (IFASD)*, 25-28 June, Como, 2017.

8. Han, C.H., Yun, C.Y., Kim, S.J. and Jung, S.N., "Aeromechanical Stability Investigation of a Composite Hingeless Rotor in Hover," *Journal of the American Helicopter Society*, Vol. 48, 2003, https://doi.org/10.4050/JAHS.48.159.

9. Lütke, B., Nuhn, J., Govers, Y., and Schmidt, M., "Design of a rotor blade tip for the investigation of dynamic stall in the transonic wind-tunnel Göttingen," *The Aeronautical Journal*, Vol. 74:(1232), 2016.

10. Müller, M.M., Schwermer, T., Mai, H., and Stieg, C., "Development of an innovative double-swept rotor blade for the rotor test facility Göttingen," *DLRK 2018 - Deutscher Luft- und Raumfahrtkongress, DGLR - Deutsche Gesellschaft für Luft - und Raumfahrt - Lilienthal-Oberth e.V., Friedrichshafen*, 4-6 September, URL https://elib.dlr.de/122702/.

11. Müller, M., Weiss, A., and Braukmann, J. N., "Dynamic Stall Investigation on a Rotating semi-elastic Double-swept Rotor Blade at the Rotor Test Facility Göttingen," *Proceedings of the 78rd Annual Forum of the American Helicopter Society*, Fort Worth, 2022.

12. Lütke, B., "Dynamic Stall on a Pitching Double-Swept Rotor Blade Tip," *Diss.*, Technische Universität München, 2017.

13. Kaufmann, K., Müller, M., and Gradner, A., "Dynamic stall computations of double-swept rotor blades," In: Dillmann, A., Heller, G., Krämer, E., Wagner, C., Tropea, C., Jakirlic, S. New results in numerical and experimental fluid mechanic XII: contributions to the 21st STAB/DGLR symposium Darmstadt, Germany, 2018, *Notes on Numerical Fluid Mechanics and Multidisciplinary Desgin*, vol 142, pp. 351–361, https://doi.org/10.1007/978-3-030-25253-3-34.

14. Wolf, C. C., Braukamnn, J. N., and Müller, M. M., "Tip vortex study of a rotor with double-swept blade tips," *Proceedings 48th European Rotorcraft Forum*, Winterthur, Switzerland, 6–8 September, 2022.

15. Weiss, A., Geisler, R., Schwermer, T., Yorita, D., Henne, U., Klein, C., and Raffel, M., "Single-shot pressure-sensitive paint lifetime measurements on fast rotating blades using an optimized double-shutter technique," *Experiments in Fluids*, Vol. 58(9), 2017.

16. Weiss, A., Geisler, R., Müller, M.M., Klein, C., Henne, U., Braukmann, J.N., and Letzgus, J., "Dynamic-stall measurements using time-resolved pressure-sensitive paint on double-swept rotor blades," *Experiments in Fluids*, Vol.63(15), 2021, https://doi.org/10.1007/s00348-021-03366-6.

17. Schwermer, T., Richter, K., and Raffel, M., "Development of a rotor test facility for the investigation of dynamic stall," *New Results in Numerical and Experimental Fluid Mechanics X, Springer*, Vol. 6(7), 2016, pp. 663–673.

18. Goerttler, A., Braukmann, J., Schwermer, T., Gardner, A., and Raffel, M., "Tip-Vortex investigation on a rotating and pitching rotor blade," *Journal of Aircraft*, Vol. 55(5), 2017, DOI 10.2514/1.C034693.

19. Schwermer, T., Gardner, A., and Raffel, M., "Dynamic Stall Experiments on a Rotor with High Cyclic Setting in Axial Inflow," *Proceedings of the 73rd Annual Forum of the American Helicopter Society*, 9-11 Mai, Fort Worth, Texas, 2017.

20. Braukmann, J., Schwermer, T., and Wolf, C., "lnvestigation of young blade-tip vortices at a rotor test facility using stereoscopic PIV," *Fachtagung "Experimentelle Stroemungsmechanik"*, 5-7 September, Karlsruhe, 2017.

21. Sugimoto, T., Sugioka, Y., Numata D., Nagai, H., Asai, K., "Characterization of frequency response of pressure-sensitive paints," *AIAA Journal of Aircraft*, Vol.55(4), 2017, pp. 1460–1464, https://doi.org/10.2514/1.J054985.

22. Gößling, J., Ahlefeldt, T., Hilfer, M., "Experimental validation of unsteady pressure-sensitive paint for acoustic applications," *Experimental Thermal and Fluid Science*, 2020, https://doi.org/10.1016/j.expthermflusci.2019.109915.

23. Geisler, R., "A fast double shutter system for CCD image sensors," *Measurement Science and Technology*, vol.25(2):025404, 2014, https://doi.org/10.1088/0957-0233/25/2/025404.

24. Geisler, R., "A fast double shutter for CCD-based metrology," In: *Shiraga H, Etoh TG (eds) Selected papers from the 31st international congress on high-speed imaging and photonics*, SPIE, Osaka, vol.10328, p. 1032809, 2017, https://doi.org/10.1117/12.2269099.

25. van der Wall, B. G., "Grundlagen der Hubschrauber-Aerodynamik," *Springer, Heidelberger Platz 3, Berlin*, 2015.

26. van der Wall, B. G., "Grundlagen der Dynamik von Hubschrauber-Rotoren," *Springer, Heidelberger Platz 3, Berlin*, 2018.